Intensified swirling reactor for the dehydrogenation of LOHC

Intensified Swirling Reactor for the Dehydrogenation of LOHC

Laurens Van Hoecke[1], Nithin B. Kummamuru [1], Hesam Pourfallah[1], Sammy W. Verbruggen[1], Patrice Perreault[2, 3]

1: Sustainable Energy, Air and Water Technology, Department of Bioscience Engineering, University of Antwerp, Groenenborgerlaan 171, 2020 Antwerp, Belgium.

2: Faculty of Science, IMDO, University of Antwerp, Groenenborgerlaan 171, 2020 Antwerp, Belgium.

3: Blue App, Olieweg 97, 2020 Antwerp, Belgium

Journal: International Journal of Hydrogen Energy

Highlights

- A new swirling reactor is introduced for H_2 release of perhydro dibenzyltoluene.
- The cold flow mock-up study shows fluidization of the catalyst beads.
- Presence of the gas phase is crucial in fluidization of the catalyst bed.
- A method for simulating three phase flows with open-source software is presented.

Abstract

In the recent advances towards more sustainable global energy supply, H_2 is a possible alternative for large scale energy storage. In this view, Liquid Organic Hydrogen Carriers (LOHC) are a class of molecules that allow for easier long term energy storage compared to conventional H_2 technologies. CFD simulations were used to showcase the hydrodynamics of the dehydrogenation of a LOHC in a new reactor unit, via a cold flow mock-up study. This reactor was designed to allow for a swirling motion of the liquid carrier material, favouring the removal of H_2 gas from the flow and forcing the equilibrium of the reaction towards dehydrogenation, as well as to keep the catalyst particles in motion. The CFD simulations were validated qualitatively with experimental operation of the reactor, in a system with identical dimensionless numbers (Reynolds and Stokes), in order to use less costly products during the prototyping phase.

Keywords: Computational Fluid Dynamics, Liquid Organic Hydrogen Carrier, Dehydrogenation reactor design, Swirling fluidized bed.

Nomenclature

Abbreviations

Ar	Archimedes Number
BT	Benzyltoluene
CFD	Computational Fluid Dynamics
DBT	Dibenzyltoluene
DoD	Degree of Dehydrogenation
Eo	Eötvös Number
H18-DBT	Perhydro-dibenzyltoluene
LOHC	Liquid Organic Hydrogen Carriers
LPM	Litre Per Minute
Re	Reynolds Number
SST	Shear Stress Transport

Roman

g	Gravitational Acceleration
f	Distorted Particle Model Parameter
k	Turbulent Kinetic Energy
p	Pressure
t	time
s	Sphericity
C	General Coefficient
D	Diameter
F	Momentum Exchange Source Term
U	Velocity

Greek

α	Volume Fraction
ϵ	Void Fraction
μ	Dynamic Viscosity
ρ	Density
σ	Surface Tension
τ	Stress Tensor
ϕ	Schaeffer Model Coefficient

Subscripts

d	Dispersed phase
g	Gas phase
i	General phase
j	Coupled phase
l	Liquid phase
m	Mixture
mf	Minimal fluidization
s	Solid phase
DP	Distorted Particles
SC	Spherical Cap
SP	Spherical Particles
WY	Wen & Yu

Superscripts

D	Drag
VM	Virtual Mass
TD	Turbulent Dispersion

1. Introduction

Hydrogen has been gaining increased attention as a potential alternative to fossil fuels since it can be a new and sustainable energy vector. The critical issue with H_2 is finding effective methods to store the fuel. Many potential methods for H_2 storage have been proposed in the past, of which the storage in Liquid Organic Hydrogen Carriers (LOHC) is an especially promising storage method, especially for long term / long distance transportation [1, 2]. H_2 is stored in a LOHC molecule by chemically bounding it to available sites on the carrier molecule, e.g., the carbon – carbon double bonds on a homocyclic (e.g., BT, DBT, toluene, biphenyl/diphenyl methane [3], light cycle oil from fluid catalytic cracking [4]) or heterocyclic aromatic (e.g., biphenyl/diphenyl methane [3], mono and dimethyl-quinolines [5, 6], as well as substituted quinolines and pyridines [7, 8]) , or even on aliphatic oxygen-containing molecules (e.g., furfuryl alcohol [9], biphenyl and diphenyl ether [10]). H_2 can be released by reversing the process, thus leaving the LOHC molecule to be reused to store to new hydrogen.

It is this H_2 release step that has proven to be one of the major challenges in the overall storage cycle for LOHC, due to the high dehydrogenation enthalpy required (ΔH_0 = 65 kJ mol^{-1}_{H2}) at high temperatures (≈ 300 °C) [11]. During the dehydrogenation, the catalyst is deactivated by the liquid products, as well as in the case of catalyst particle de-wetting due to the considerable amounts of H_2 formed [12]. To improve the efficiency of the process, and to minimize decomposition of the LOHC during repeated hydrogenation/dehydrogenation cycles, much research has been dedicated to finding efficient catalysts for LOHC[13-17], as well as identifying alternative LOHC molecules[3-10]. Much less effort has been put in the study of innovative reactor concepts. A review by Modisha et al. also highlighted the importance of improved reactor design for LOHC dehydrogenation, where the need for increased mass and heat transport towards the catalyst surface is of critical importance [18]. Several reactor concepts have been described in the literature and were recently highlighted in a current opinion article [19]: Laboratory studies focusing on the operational conditions of LOHC hydrogenation or dehydrogenation process, often rely on batch reactors. These studies include hydrogenation of DBT using a gas phase of non-pure hydrogen, such as the addition of water vapours from electrolysis [20], or hydrogenation experiments with H_2/CO_2 mixtures [21] where they showed that hydrogenation of DBT is possible without the need for pure H_2 gas flow. Another operational concept that was shown using a batch reactor was that of a hot pressure swing reactor. This process showed that DBT can be effectively hydrogenated and dehydrogenated in the same reactor vessel by increasing and decreasing the H_2 pressure [22]. A second type of reactor used on laboratory scale is the spray – pulse reactor. In this reactor LOHC liquid is periodically pulsed onto a heated catalyst bed, this limits macro-kinetic transport phenomena towards to catalyst surface, allowing for fast reaction once the LOHC is sprayed onto the catalyst. These reactors have been used in LOHC research to evaluate the effectiveness of both Pt and Ni catalyst supported by activated carbon [23, 24]. A small

scale example of a continuous type reactor is the membrane reactor, these reactors are characterized by immediate removal of the formed H_2 gas, which allows for operational modes that can exceed the dehydrogenation equilibrium [25, 26]. A membrane reactor can also be used in low pressure mode, which decreases the required reaction temperature for H_2 release [27]. Reactive distillation operated at low pressure to decrease the dehydrogenation temperature, as well as favouring the H_2-rich LOHC/catalyst contact have been proposed [28, 29], leading however to a complex design due to the close volatilities of the H_2-rich and H_2-lean LOHC. In an attempt to supply the dehydrogenation heat directly in the dehydrogenation unit, heat pipe concepts have been proposed. It was showed that the critical design factor was ensuring a homogeneous dehydrogenation temperature by placing either a phase change material, or a porous metallic material between the burner and the dehydrogenation section [30, 31]. A recent patent discloses the invention of a centrifugal dehydrogenation reactor based on a heat pipe exchanger to supply the dehydrogenation heat. They describe the simultaneous H_2 separation from the catalyst surface by applying a centrifugal acceleration [32]. The catalyst is coated on surface of the external walls of the down-flowing centrifugal device. It is interesting to note that if density-based separation occurs during centrifugal separations, then the unit is counterproductive as the H_2-rich LOHC is lighter than its dehydrogenated counterpart, then positioned favourably near the catalytically coated wall. Even though various dehydrogenation reactors have been described, only the tubular case has been applied commercially [33, 34]. This commercial reactor is designed as a horizontally placed tubular reactor partly filled (up to 80 % of the reactor volume) with LOHC and catalyst pellets. This allowed for a headspace in which H_2 could escape the reaction medium without affecting the required catalyst-LOHC contact time [35]. Interestingly, Heublein et al. [12] characterized the heat transfer and productivity of a tubular reactor operated in counter- and co-current mode, with horizontal and vertical orientations, and demonstrated the superiority of the vertical operations.

In this work, we introduce a new swirling reactor concept for LOHC dehydrogenation for free-flowing commercial dehydrogenation catalysts and investigate the hydrodynamics of the liquid-solid-gas flow in the reactor, using a combination of CFD simulations and cold flow mock-up system with water, glass beads and argon. Swirling flows in reactors are known to intensify local heat and mass transfer, [36] which is highly beneficial in the case of LOHC dehydrogenation due to the high thermal input, as well as loss of catalyst productivity when H_2 is not efficiently removed from the surface of the catalyst. The proposed swirling unit ensures that the catalyst bed is fluidized, a key aspect for dehydrogenation of DBT; that was recently outlined by Solymosi et al. [37] where they show that the use of mechanical agitation could enhance mass transfer by a factor 50 and trigger nucleation at the surface and in the pores of the catalyst.

2. Methodology

2.1 Dehydrogenation Reactor

The setup for the reactor is depicted on Figure 1. On a) the piping system is shown, with the required storage tanks, valves, the pump, and the position of the reactor. This distance between the two 200 L storage tanks measured is roughly 3 meters. The pump was an Iwaki magnet drive pump capable of 250 LPM flow rate, flow was measured using a Prosonic 91 W flow sensor. Stainless steel tubing was combined with flexible plastic tubing. Figure 1b shows the quartz prototype of the reactor, which had a total height of 600 mm and a maximal diameter of 300 mm. The reactor is based on a concept with three distinct zones. The first zone is the reaction zone (the lowest section of the reactor), with a diameter of 150 mm and a height of 150 mm, the inlets are placed tangentially on the walls of this section of the reactor. These inlets are 25.4 mm ID pipes that form an angle of 10 degrees with the horizontal plane. In this reactive zone, the catalyst bed is present, and this is the area where the hydrogen release will happen from the LOHC liquid.

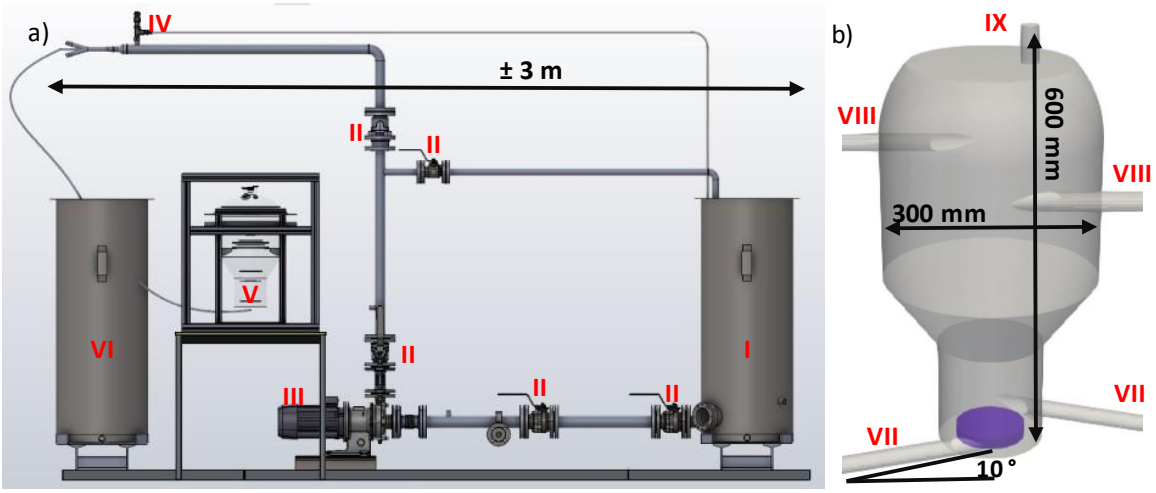

Figure 1 a) Overview of the reactor setup. I: 200 L tank containing liquid to be sent to the reactor. II: valves: III: pump. IV: pressure relief valve. V: Reactor. VI: 200 L tank containing liquid after passing the reactor. b) Details of the geometry of the reactor. VII: The liquid inlets. VIII: The liquid outlets. IX: the gas outlet. The blue disc represents the position of the fritted disc.

Since this setup is currently build as a cold flow prototype, gas will be introduced via a fritted disc placed at the bottom of the reactor. The main goal of this reactor is to generate swirling flow patterns within the reactive zone, which will intensify local heat and mass transfer [36]. This is highly beneficial in the case of LOHC dehydrogenation: the reaction requires a high thermal input and due to its endothermicity, the catalyst particles tend to decrease in temperature during the reaction. Increased mass transfer is also beneficial to remove the formed H_2 from the pores and surface of the catalyst particles. An expansion zone was designed after the reactive zone, where the diameter increased from 150 mm to 300 mm. The height of this zone is 100 mm. In the expansion zone the velocity will

decrease, causing solids to fall down back into the reactive zone. Finally, the top section of the reactor which function as a disengagement section is 300 mm in height with the upper 100 mm section rounded. This rounded top has three openings one for the outlet of the gas, and two openings for probes, each outlet has a height of 50 mm. Only the opening for the gas is depicted here and used in the initial CFD – simulations. At a height of 380 mm from the bottom, two more 25.4 mm ID outlets for the liquid are situated tangentially from the wall parallel to the horizontal plane. We would like to stress that the design of this reactor is an initial prototype, used to show the fluidization of glass beads in presence of gas in swirling flows. The different sections of the reactor are overdimensioned to ensure that the beads will remain in the reactor and to study the separation behaviour of the gas in the swirling flows.

2.2 Cold flow mock-up strategy

We designed a pre-pilot LOHC test rig allowing to dehydrogenate up to 250 LPM. The process was designed for the dehydrogenation of either BT or DBT, dehydrogenated using the commercial eggshell 0.3 wt.% Pt catalyst supported on 2 mm alumina beads (Clariant). The choice of BT and DBT is based on their relatively high H_2 storage capacity, 6.2 wt.% and 56 g L^{-1}, excellent thermal properties, a good (eco)toxicological profile and technical availabilities (commercial heat transfer fluid) [38-40], even though not comparable to the large quantities required by a future H_2 economy. BT has a lower viscosity, but a lower boiling point and increased vapour pressure compared to DBT, thus less suited for the operational conditions inside the proposed reactor, where a large liquid free surface is expected. This would cause more evaporation of the BT LOHC compared to the DBT counterpart [15].

The pre-pilot facility can be heated up to 300 °C using an induction heating system and can be operated up to 3 bars (quartz reactor). However, as a first experimental concept, we decided to mimic this reacting system using simplified relationship based on dimensionless groups, a method commonly used for fluidized beds, especially for catalytic applications [41]. We followed the philosophy of Knowlton et al. [42] as they showed that such scaling relations are most relevant for cold flow model used to improve the operation of an existing plant, versus for scale-up purposes. As the design and scale-up of swirling fluidized bed is still at its infancy, especially for liquid-gas-solid applications, where to the best of the authors knowledge, no such procedure has been proposed, we decided to minimize the risk related to the reactor design by relying on such similarities.

We retained the Reynolds & Stokes similarities, and maintained the centrifugal acceleration imposed on the solid phase by the liquid. We also imposed water at 20 °C as the working fluid. The set of scaling relations used is thus composed of the Reynolds & Stokes dimensionless groups, imposing the fluid velocity and water as the working fluid. By doing so, the density of the particulate phase has to be

around 2900 kg m^{-3}, with a 1.5 mm diameter. We thus selected glass beads (2500 kg m^{-3}) in the 1.5 - 2 mm diameter range. To further strengthen this correlation we looked at the onset of fluidization as described by Wen and Yu in the book by Fan for spherical particles in liquid – solid fluidized beds [43].

$$U_{mf0} = \frac{\mu_l \cdot \sqrt{33.7^2 + 0.0408 \cdot Ar} - 33.7}{\rho_l \cdot d_p} \qquad Eq.1$$

With Ar the Archimedes number defined as [44]:

$$Ar = \frac{d_p^3 \cdot \rho_l \cdot (\rho_s - \rho_l) \cdot g}{\mu_l^2} \qquad Eq.2$$

We used this relation where we assumed the value for minimal fluidization velocity ϵ_{mf} as 0.5 and spherical particles, i.e., the sphericity (s) as 1, to calculate the minimal fluidization velocities for both the real case of H18-DBT fluidizing porous Al_2O_3 beads and water being used to fluidize glass beads. We found that U_{mf} for H18-DBT was 0.017 m s^{-1} and for water this value resulted in 0.015 to 0.021 m s^{-1} depending on the particle diameter (1.5 – 2 mm). This fluidization calculation is valid for bottom fed fluidized beds and does not consider the influence of gas phase. The close similarity in U_{mf} between the cases does provide some confidence that the results of the cold flow mock-up will give general trends that can be applied to a reactive system. In the work by Fan it is shown that the addition of gas to a liquid based fluidized bed will reduce the U_{mf} [43], the influence of the thermophysical parameters of the gas is however not further studied in our work.

The mass of catalyst beads was estimated from the molar catalyst to LOHC ratio (Jorschick et al.. [22]). We assumed our catalyst mass to be the same as the amount of catalyst used in their batch reactor experiments, by using the same ratio of 6667 mol H18-DBT per mol Pt. In our 25 L system with H18-DBT heated to 573 K, this would result in a total mass of around 600 g. Due to the Reynolds and Stokes similarities, we assumed the mass of Al_2O_3 based catalyst particles to be the same as the mass of glass beads required.

To further mimic the dehydrogenation of LOHC, we generated a stream of diffused argon using a porous fritted disc, with a diameter of 100 mm and thickness of 18 mm (Hailea, model-ASC-100) from the lower part of the reactive section of the dehydrogenation unit. To simulate the H_2 produced during dehydrogenation, we extracted the maximum H_2 production rate from the same published data of Jorschick et al. [22] used to estimate the amount of beads. Using their published data, 10 LPM of argon was continuously fed to the fritted disk.

This figure was estimated from the maximal slope of the work by Jorschick on the second dehydrogenation cycle of the fifth figure in his work [22]. We extracted a slope and then converted it to a productivity of $2.34 \cdot 10^{-4}$ Nm^3_{H2} g^{-1}_{LOHC} h^{-1}. The maximal value of this curve was used since the experiments performed by Jorschick were done in a batch reactor and in our system, there is a constant influx of new H18-DBT. We assumed further that only 2/3 of our reactive zone would contain catalyst beads at a given time, so using this volume we calculated the mass of H18-DBT to 1.3 kg, (using density correlations extracted from the work of Aslam extracted for 573 K [45]). Using these relations, we calculated the volume of H_2 released and corrected this for a dehydrogenation temperature of 573 K, this corresponded to a value of $1.77 \cdot 10^{-4}$ m^3 s^{-1} or 10.6 LPM. For practical purposes of available mass flow controllers, we rounded this value down to 10 LPM.

2.3 CFD Simulation Models

2.3.1 Governing Equations

The CFD simulations are performed using OpenFOAM's multiphaseEulerFOAM solver (OpenFOAM version 8). The solver is based on the Euler-Euler approach for modelling multiphase systems. This approach is based on the idea of interpenetrating continuums, with each continuum described by its own continuity and momentum equation. The continuity equation is:

$$\frac{\partial}{\partial t}(\alpha_i \rho_i) + \nabla \cdot (\alpha_i \rho_i \boldsymbol{U}_i) = 0 \qquad Eq. 3$$

Where α_i is the volume fraction of phase i, ρ_i is the density and $\boldsymbol{U_i}$ is its velocity. The momentum equation of each phase is defined as:

$$\frac{\partial}{\partial t}(\alpha_i \rho_i \boldsymbol{U}_i) + \nabla \cdot (\alpha_i \rho_i \boldsymbol{U}_i \boldsymbol{U}_i) = -\alpha_i \nabla p + \nabla \cdot (\alpha_i \tau_i) + \alpha_i \rho_i g + F_{ji} \qquad Eq. 4$$

With p is the pressure shared between the phases, τ_i denoting the stress tensor,g represents the gravitational acceleration and F_{ij} denoting the momentum exchange from phase *j* on phase *i*. This momentum exchange can include drag, lift, wall lubrication, virtual mass, and turbulent dispersion. In line with the work from Hu et al. [46] for three phase simulations, only the contributions from drag, virtual mass and turbulent dispersion are included. For this cold flow mock-up study the energy equation was not considered in the simulation.

2.3.2 Drag Correlation

Due to the low abundance of gas and solid phases when compared to liquid phase, it is assumed that both the gas – liquid and solid – liquid system are dispersed – continuous phase, with the liquid phase being the continuous phase. The drag force exerted between the gas – liquid and solid – liquid phases can then be expressed as:

$$F_{il}^{D} = C_{dl}(U_d - U_l) \qquad Eq.5$$

With d representing the dispersed phase (gas or solids) and l the liquid phase. C_{dl} represents the specific drag correlation for each of these cases.

The drag correlation for the gas – liquid system is calculated according to the model of Ishii and Zuber.[47] This drag correlation considers three different flow regimes: a dense spherical particle regime, a dense distorted particle regime and a dense spherical cap regime.[48, 49] These are accounted for by the following formulas:

$$C_{SP}\begin{cases} = 24 \cdot \dfrac{(1 + 0.1Re_m^{0.75})}{Re_m} & with\ Re_m \leq 1000 \\ = 0.44 & with\ Re_m > 1000 \end{cases} \qquad Eq.6$$

In this formula the expression for Re_m is given by [50]:

$$Re_m = \frac{\rho_l \cdot |U_g - U_l| \cdot d_g}{\mu_{mix}} \qquad Eq.7$$

With d_g the diameter of the gas bubble and μ_{mix} the dynamic mixture viscosity that is calculated by:

$$\mu_{mix} = \mu_l \cdot (1 - \alpha_g)^{-2.5 \cdot \frac{\mu_g + 0.4\,\mu_l}{\mu_g + \mu_l}} \; with \max\,(1 - \alpha_g) < 0.001 \qquad Eq.8$$

The second case for distorted particles (or bubbles) is defined as

$$C_{DP} = \frac{2}{3} \cdot \frac{1 + 17.67\, f^{6/7}}{18.67 \cdot f} \cdot \sqrt{Eo} \qquad Eq.9$$

With *f* defined as:

$$f = \min\left(\frac{\mu_l}{\mu_{mix}} \cdot \sqrt{1 - \alpha_g}, 1e^{-03}\right) \qquad Eq.10$$

And with Eötvös number (Eo) is the ratio of the gravitational forces and the surface tension (σ):

$$Eo = \frac{g(\rho_l - \rho_g)d_g^2}{\sigma} \qquad Eq.11$$

The drag coefficient for the dense spherical cap bubble regime is defined as:

$$C_{SC} = \frac{8}{3} \cdot \left(1 - \alpha_g\right)^2 \qquad Eq. 12$$

The solid – liquid drag interaction was calculated by the Gidaspow drag correlation model. This model is a combination of the Ergun and Wen & Yu drag models. The Ergun drag model is used if the volume fraction, $\alpha_l \leq 0.8$, and the Wen & Yu correlation is used when the volume fraction of the continuous phase exceeds 0.8 [51].

The Ergun term is given by [52]:

$$C_{SL} = 150 \cdot \frac{\alpha_s(1-\alpha_l)\mu_l}{\alpha_l d_s^2} + \frac{1.75\rho_l\alpha_s|\boldsymbol{U_s} - \boldsymbol{U_l}|}{d_s} \qquad Eq. 13$$

The Wen & Yu drag correlation is as follows [53]:

$$C_{SL} = \frac{3}{4} C_{WY} \frac{\alpha_s\alpha_l\rho_l|\boldsymbol{U_l} - \boldsymbol{U_s}|}{d_s} \alpha_l^{-2.65} \qquad Eq. 14$$

With the value C_{WY} [46]:

$$C_{WY} \begin{cases} = \frac{24}{Re}[1 + 0.15Re^{0.687}] & with\ Re < 1000 \\ = 0.44 & with\ Re \geq 1000 \end{cases} \qquad Eq. 15$$

2.3.3 Virtual Mass

The virtual mass is the term that accounts for the inertia induced in the system by the deflection of mass caused by an accelerating (or decelerating) object in the fluid. The model for a constant coefficient of virtual mass was selected based on the work by *Hu* et al. [46]:

$$F_{gl}^{VM} = C^{VM}\alpha_g\rho_l\left(\frac{DU_g}{Dt} - \frac{DU_l}{D_t}\right) \qquad Eq. 16$$

For the gas – liquid interaction the constant coefficient used was $C^{VM} = 0.5$. The virtual mass interaction was not accounted for in the solid – liquid phase pair, C^{VM} used was set to 0 in the latter case.

2.3.4 Turbulent Dispersion

The turbulent dispersion forces represents the diffusion of the turbulent kinetic energy of the dispersed phase caused by the presence of the continuous phase eddies [54]. This interaction like the

virtual mass is only accounted for in the gas – liquid phase pair. The specific momentum exchange term is given by:

$$F_{gl}^{TD} = C^{TD}\alpha_g \rho_l k_l \nabla \alpha_g \qquad Eq.17$$

The turbulent dispersion coefficient C^{TD} was kept constant at 1.0, the symbol k_l represents the turbulent kinetic energy of the liquid [46].

2.3.5 Turbulence Model

In this study the RANS type k-Omega SST (Shear Stress Transport) turbulence model of Menter [55] was used for the liquid phase, since it has shown good results with swirling flows [56]. The dominant flow inside the reactor will be the liquid phase, therefore it was opted to reduce the computational complexity by turning the turbulent contributions of the gas flow off. To account for the solid particles in the flow, the kinetic theory of granular flow was used (Table 1).

Table 1: Settings, models and parameters used for the simulations.

	Operational Parameters
Particle Density	2500 kg m^{-3}
Particle Diameter	1.5 mm – 2 mm
Total Particle mass	0.600 kg
Water Density	1000 kg m^{-3}
Water dynamic viscosity	$1.05 \cdot 10^{-3}$ Pa·s
Water surface Tension	0.07 N m^{-1}
Gas Density	Calculated by ideal gas law
Gas dynamic viscosity	$2.1 \cdot 10^{-5}$ Pa·s
Gas influx rate	$3.14 \cdot 10^{-4}$ kg s^{-1}
	Boundary Conditions
Water inlet flow rate	$4.165 \cdot 10^{-4}$ m^3 s^{-1}
Water inlet temperature	300 K
Outlet Pressure	$1 \cdot 10^5$ Pa
Fluid – Wall Interaction	No – Slip Condition
Solid – Wall Interaction	Johnson Jackson Particle Velocity
	Restitution Coefficient 0.2
	Specularity Coefficient 0.1
	Turbulence Models
Water turbulence model	K – omega SST
Gas turbulence model	none
	Kinetic Theory Conditions
Max packing limit	0.65
Max frictional limit	0.5
Viscosity Model	Syamlal model
Conductivity Model	Syamlal model

Granular pressure model	Syamlal, Rogers & O'Brien model
Frictional stress model	Schaeffer model ϕ = 36
Radial model	Carnahan & Starling Model
	Interfacial Exchange Models
Solid – liquid drag model	Gidaspow
Gas – liquid drag model	Ishii & Zuber
Gas – liquid Virtual Mass model	Constant Coefficient model
Gas – liquid Turbulent Dispersion model	Constant Coefficient model

3. Results and discussion

3.1 Computational Domain

The computational domain for the comparison with the experimental work is a simplified geometry of the real reactor: the studied area of the reactor was limited to a height of 450 mm of the original 600 mm height. This limited height corresponded to a total volume of the reactor of 21.3 L. This approach was selected so that there was less computational effort required to resolve the gas – liquid interphase, a known computationally expensive phenomenon [57] that does not contribute, here, in the overall results of the simulation, since we are mostly interested in the interactions of the liquid gas and solids near the bottom of the reactor. The height of 450 mm was chosen to be below the gas – liquid interphase near the top of the reactor, as can be seen in Figure 2. The height of this gas-liquid interphase is dependent on the flow rate and was found to follow the trends observed for the liquid level in the reactor as a function of time for various inlet flow rates (Figure 3). These results were obtained from a Volume of Fluid (VOF) simulation for simplicity on a mesh created for the full reactor. Numerical implementation of VOF in OpenFOAM is well explained in a work from Larsen et al. [58]. From this we can conclude that with an inlet flow rate of 75 LPM the water volume caps at 25.9 L, when the water inflow reaches steady state. This justifies the use of the mesh with a capped upper section, with the entire computational domain filled up with water.

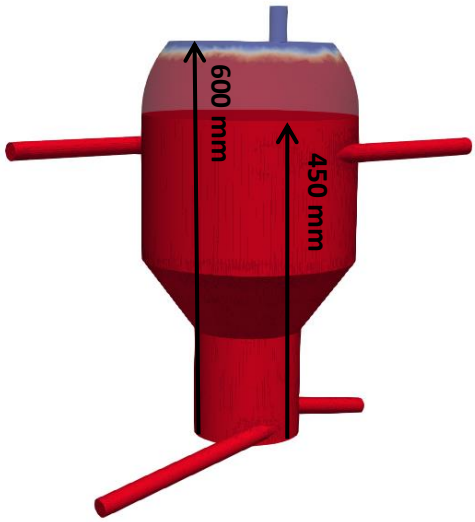

Figure 2 Steady state water volume at 60 s. The translucent part denotes the water level in the full reactor (obtained by VOF). The opaque section is the portion of the geometry used in the Eulerian simulations.

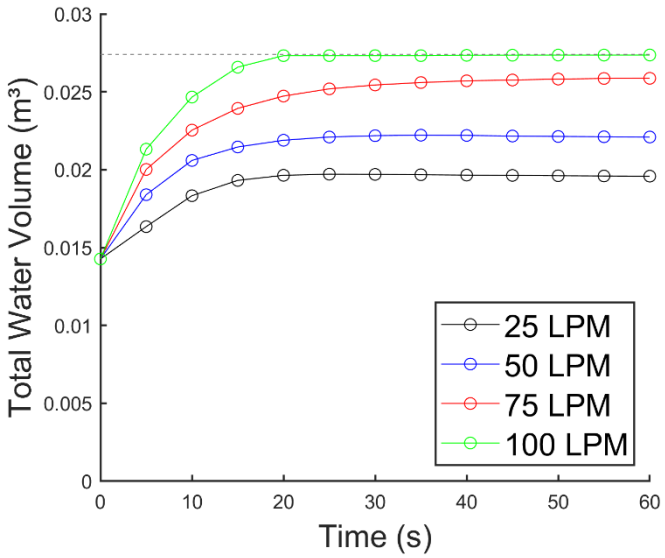

Figure 3 Steady state water volume obtained by VOF simulations. The dotted grey line denotes the total reactor volume. At 75 L min^{-1} total inlet flow rate a high inlet flow rate was achieved without overflowing the reactor.

For the three phase Eulerian simulations we introduced the water in the system from the inlets at flow rates of 50 LPM for comparison with our experimental work, or 75 LPM for other simulations. As this was close to the maximal achievable flow rate within the reactor. A mass of 0.6 kg of glass beads was initialized near the reactor inlet. The argon gas was introduced with a flow rate of 3.95 kg s^{-1} via a source term. The active volume in the mesh for this source term was chosen to correspond to the same volume of the fritted disc that was used in the experiment, see also figure 1. The parameters used to describe the different phases can be found in Table 1.

On this capped geometry a mesh independent study was performed. This mesh independence study used the Grid Independence Index (GCI) approach from Roache (1994) [59] and is explained in full in

a recent work published by our group [60]. The results of this grid independence study can be seen in Figure 4.

For this study, three meshes with different refinement levels were used, coarse: 464 780 cells, medium: 1 478 514 cells and fine: 4 689 241 cells. The results are obtained after 3 seconds of simulated time, with 0.6 kg of solids present. The initial particle bed height amounts to 32 mm. Boundary conditions for this case can be found in Table 1. Solids were introduced into the computational domain in a cylinder with a 32 mm height and 148 mm diameter. Gas was being generated by a semi-implicit source term in a cylinder of 100 mm diameter and 18 mm height, i.e., with the same dimensions as the fritted disc used in the cold flow experiments. The results show a converging behaviour between the three meshes, as demonstrated by the extrapolated line, calculated from the approach by Roache [59]. The profile of the azimuthal velocity of the medium mesh, fits that of the extrapolated curve, and with an underprediction of 4 % of the maximal azimuthal solid velocity. This was deemed to be sufficient accuracy for the simulations since computational time required for the medium mesh was about five times shorter when compared to the fine mesh.

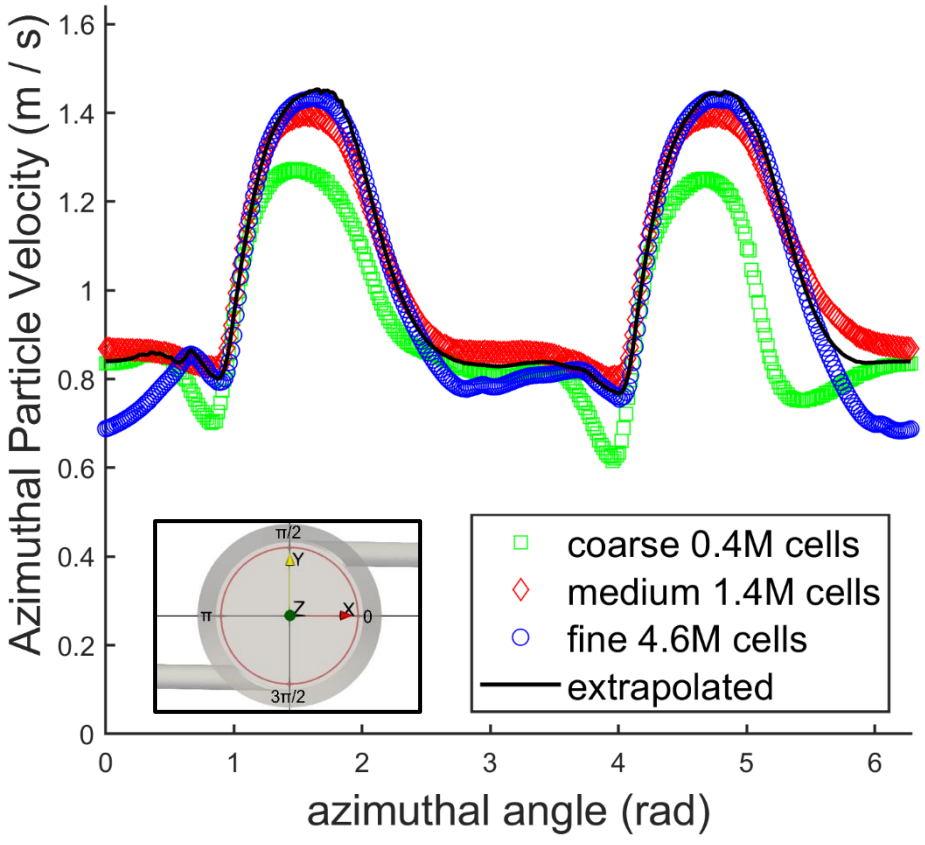

Figure 4 Azimuthal velocity of the solids, extracted in a horizontal plane (10 mm height, 65 mm radius), for meshes with three different refinement levels. Inlet flow rate 75 L min-1, total mass of solids 0.6 kg. Results obtained after 3 s of simulated time. The used azimuthal angle is shown on the insert.

3.2 Fluidization Behaviour

The reactor was designed with the idea in mind to have fluidization of the beads in order to improve the mass and heat transfer rate and subsequently having a more efficient dehydrogenation of H18-DBT by removing the gas bubbles from the catalyst surface and by supplying fresh and heated H_2-rich LOHC continuously. In order to achieve this, the particles have to be dragged along by the inflowing liquid, but this behaviour should be studied in a three-phase system (liquid-gas-solid) since in the reactive application H_2 is generated at the catalyst surface during reactor. The proof that this concept is able to fluidize beads in a three-phase flow is shown in Figure 5 by the cold flow mock-up. In this figure, it is observed that when the drag is imposed on the particles without any gas, the bed expansion is minimal, as is the particle movement (Figure 5a). The CFD results confirm this trend. To do so, we plotted a contour plot of the volumetric solid fraction with a cut-off value of 0.1. We also see that the bed height is clearly visible (and comparable to the original bed height at rest at the beginning of the simulations), and only affected by the effect of the high velocity jets of entering liquid slightly upstream of the liquid inlets. This tendency is clearly confirmed by the experiments. The effect of the simulated production of H_2 gas on the fluidization is striking (Figure 5b).The injection of 10 LPM of argon results in a solid bed with an increased volume and smaller local liquid inlet effect. We can expect that the considerable volume increase of the solid bed will be highly beneficial to ensure an adequate H_2-rich LOHC-catalyst contact to allow for the dehydrogenation reaction to happen. The fluidization of the solid bed also ensures a sufficient bed agitation, thus in line with the recent findings of Solymosi et al. [37] highlighting the importance of mechanical agitation for mass transfer as well as to initiate nucleation on the catalyst. This comparison between the experimental and computation particle bed orientation shows that our CFD results can be relied upon to perform a qualitative analysis of the general trends seen from the simulation. In the remainder of this work the results will be discussed from the CFD study.

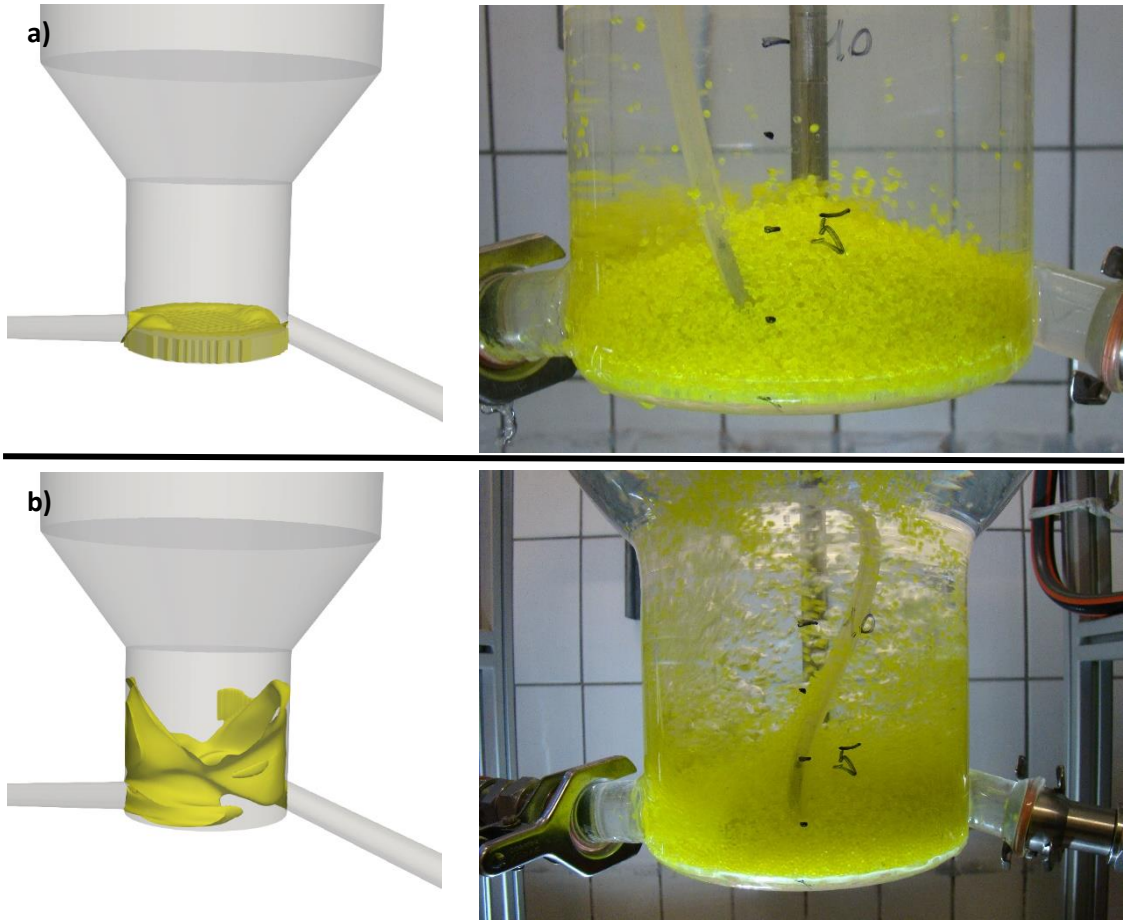

Figure 5 Comparison between simulations and experiments. a) Reactor operation without gas flow, showing little to no movement of the solid bed. b) Reactor operation with 50 LPM of water and 10 LPM gas flow, showing the fluidization of the glass beads (painted in yellow for better visualization). The cut-off value for the CFD – contour plot of the volume fraction of the solids was set to 0.15.

Figure 6 shows the height the particles can reach within the first ten seconds of operating the reactor, as seen near the wall, and analysed from our transient simulation every 2 seconds. Two interesting behaviours of the solids can be noted. First, it can be seen that the particles are dragged by the flow to heights exceeding 10 mm in the reactive zone, while still maintaining a packing density of more than 40 %. In the experimental image in Figure 5b it can be seen that particles also exceed 10 mm height, even at the lower flow rate of 50 L min^{-1} used in the experimental setup. Second, it can be seen that in the initial transient behaviour of this flow there is a certain periodicity between the black and red lines, especially in the case of 4 and 6 seconds and in the case after 8 and 10 seconds However the results after 4 and 6 seconds differ widely from those at 8 and 10 showing that this periodicity is temporary and the chaos within the flow is increasing as one would expect in a fluidized bed. This periodicity is likely caused by the symmetry of the reactor and identical inlet conditions.

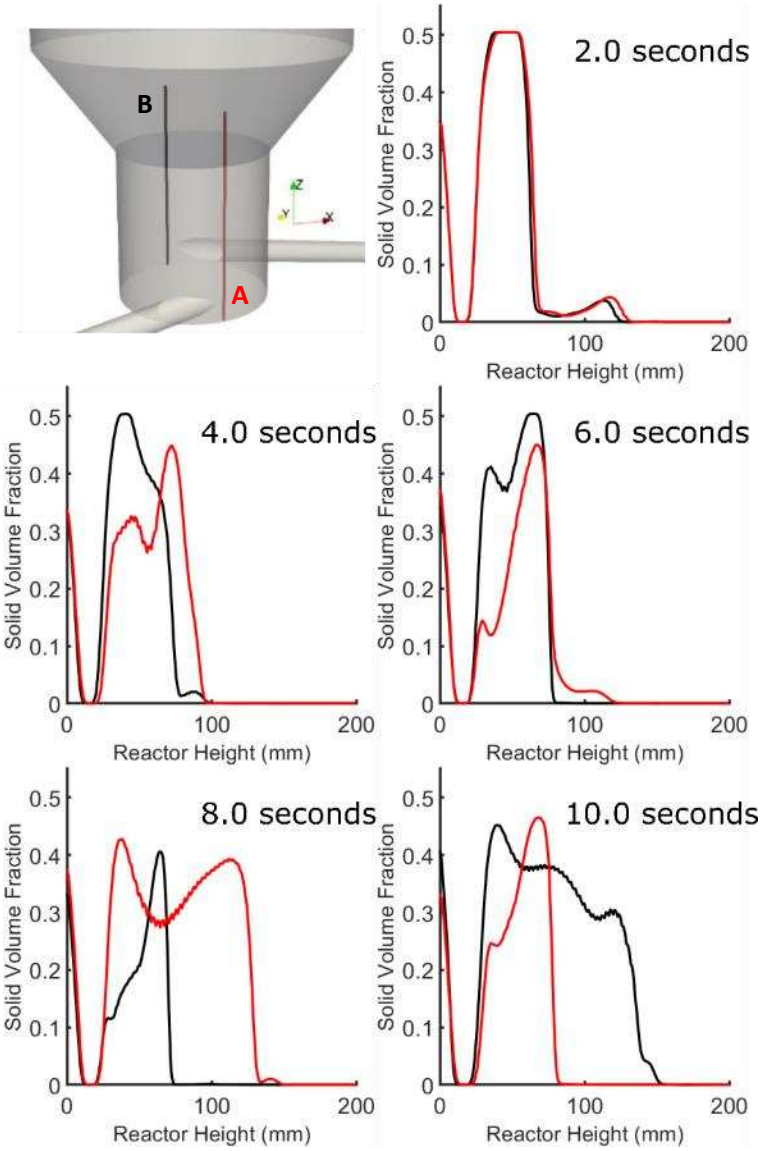

Figure 6 The evolution of the bed height near the wall over time. The red line on the graphs corresponds to position A on the front side of the reactor. The line in black corresponds to bed height at position B, at the back side of the reactor.

The position of the black and red lines are shown in the reactor (upper left). The particles achieve a height exceeding 10 mm In Figure 7a it can also be seen that the catalyst particles move upwards on the side of the walls. This figure also shows the periodicity of the flow since the movement on the walls is only visible on one side of the reactor. Notably, comparing Figure 7a with Figure 5b shows that the solids in the simulation also move up until the expansion zone in small quantities. Figure 7b shows the reactor from the bottom and here the presence of accumulated solids is noticeable. The presence of this accumulated area near the bottom of the reactor means that H_2-rich LOHC liquid comes into contact with a high concentration of catalyst beads when it is newly injected into the reactor. This is beneficial for both the reaction and for heat transfer purposes: i) the high concentration of H18-DBT in the feed favours a maximum reaction rate, and ii) this newly injected/recirculated hot LOHC act as a heat source to counteract catalyst particles cooling due to the endothermicity of the reaction. Future designs should take this into account to avoid this dead space of beads in the reactor, whilst still

keeping these beads near the inlets. In Figure 7, the absence of solid beads or low volume fraction near the inlets of the liquid is also noticeable. This is due to the high inlet velocities and will allow for easy injection of the liquid since the solid beads do not obstruct the inlets.

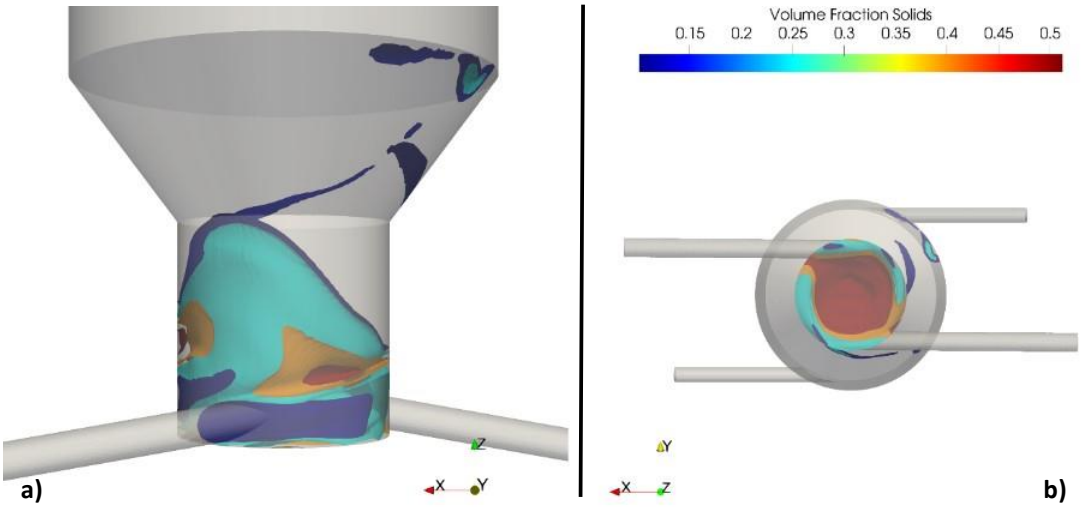

Figure 7 The envelopes of the solid fraction shown for a) the view on side and b) the view from the bottom plate (B). The envelopes show the solid volume fraction for 0.1 (blue), 0.25 (cyan), 0.4 (orange) and 0.5 (red). These images was taken from the simulation after 10 seconds.

3.3 Liquid and Slip Velocity

Next to the distribution of the solid, the behaviour of the liquid flow is critical. The streamlines of the liquid after 10 seconds of simulation can be seen in Figure 8. It can be seen that the liquid flow in the reactor is swirling in a helical upwards pattern, which is caused by the orientation of the inlets. In this figure it can be seen that the fluid velocity is higher near the walls and the inlets, reaching a velocity of 1.4 m s^{-1} in these areas.

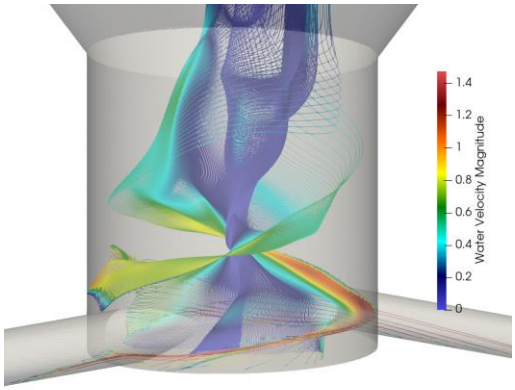

Figure 8 Streamlines of the liquid velocity in the reactive zone after 10 seconds. The flow has a helical pattern that swirls upwards and has higher velocity near the walls.

A second parameter to study the interaction between the liquid and the solid particles is the slip velocity (the difference in velocity magnitude between the solid and liquid phase). An increase in solid-liquid slip velocity is beneficial for both heat and mass transfer, both phenomena are highly advantageous for the endothermic dehydrogenation reaction where the catalyst is deactivated by the

liquid product, and where the H_2 gas bubbles tend to stay in the packed bed. Figure 9 shows the slip velocity extracted at a height of 10 mm and in a circle with a radius of 65 mm after 10 seconds of simulation. During the reactor operation the slip velocity reaches a maximal value of 0.4 m s^{-1}, and it shows positive nonzero values almost completely over the full extent of the azimuthal profile of the reactor. These data points were extracted from our simulation results, the agreement of the GCI – study in section 3.1 proves that we can rely upon these results with an estimated relative error of about 4 %.

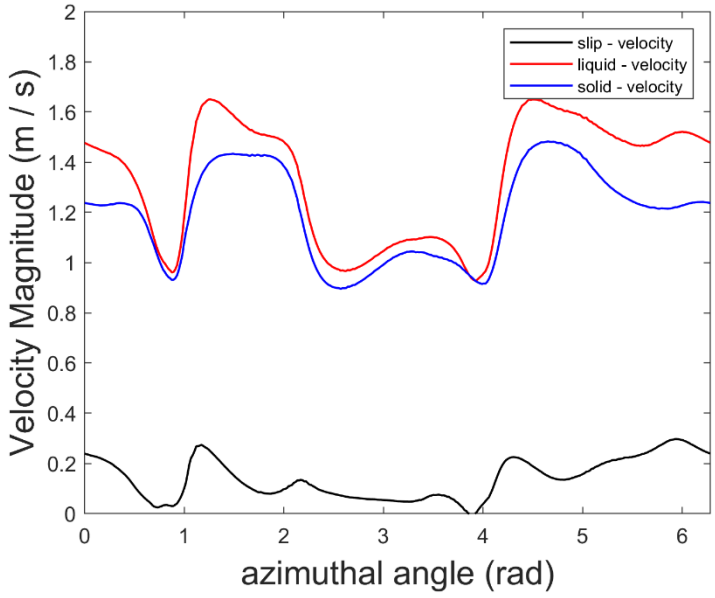

Figure 9 *Velocity profile for the liquid and solid phase, with the resulting slip velocity. Data was extracted at a height of 10 mm and a radius of 65 mm after 10 s of simulation. For the interpretation of the azimuthal angle the reader is referred to Figure 4*

3.4 Gas Distribution in the Reactor

In order to improve the reaction, a fast removal of the gas phase is required. The gas phase present around the particles can inhibit the reaction of the liquid H18-DBT by covering the surface of the catalyst particles with hydrogen bubbles, thus potentially leading to catalyst dewetting. When investigating the distribution of the gas phase it was seen that most of the gas that is generated at the bottom plate tends to remain in the centre of the reactor. This is caused by the rotational movement of the liquid, which forces the light density gas towards the centre. The reactor design proposed here shows to have a separation effect to remove the gas from the liquid flow (Figure 10). In this figure the lilac arrows show the magnitude of the gas velocity extracted from CFD simulation, with its point of origin on the central plane. These arrows show that the gas phase within the reactive zone of the reactor is also influenced by the swirling flow of the liquid. It is this effect that helps to concentrate the gas phase in the centre of the reactor.

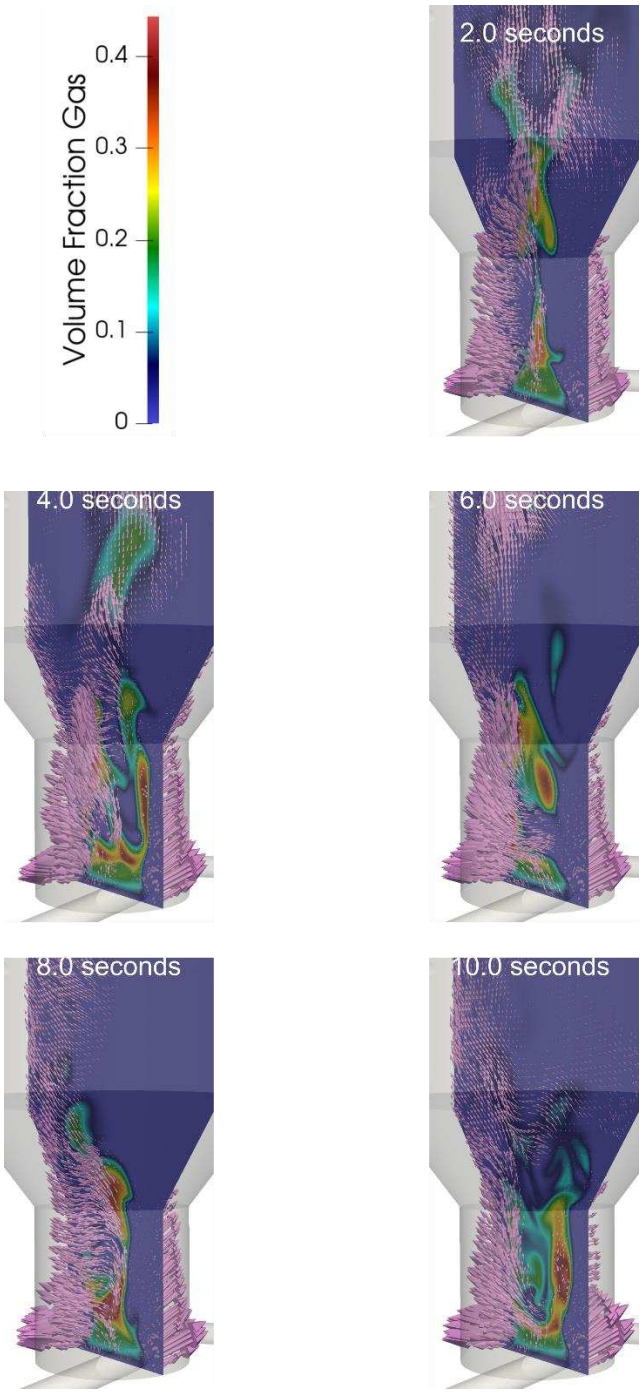

Figure 10 Central plane of the reactor showing the distribution of argon gas over the course of the simulation. The lilac arrows denote the magnitude of the gas velocity.

3.5 Future Design Changes

With this reactor we have shown the first concept that the use of a swirling fluidized bed can be applied to a system with water, glass beads and argon gas. The parameters for this three-phase system were calculated to have high similarities with H18-DBT, Al_2O_3 catalysts and hydrogen gas. This initial design is far from the optimal design, a simple calculation of the liquid hour space

velocity (LHSV) shows that with current operating parameters: 75 LPM inlet flow rate and only 0.6 kg of catalyst, the LHSV exceeds 9000 h^{-1}. This is an order of magnitude of 100 times higher than what the chart of Peters et al. [35] on the relation between LHSV and temperature is designed for, and thus gives a very low Degree of Dehydrogenation (DoD) [61]. For this reason, we suggest using a higher catalyst mass as much more catalyst can fit in our reactor. Secondly, the minimal inlet flow rate should be found where the catalyst will remain in fluidized state. Thirdly, using recirculation of the liquid is also highly recommended, and this is often used in liquid based fluidized beds [62]. Recirculation of the liquid is not advised in the current geometry and with current operating conditions. To estimate the number of recirculation passes in our system, we calculated the 1st Damköhler number for this system according to Otalvaro – Marin and Machuca – Martinez [63], with the kinetic parameters obtained from Bulgarin's work [64]. We achieved a Damköhler number of $5 \cdot 10^{-4}$, which would require over 100 passes in the reactor to achieve reasonable DoD, according to the work of Otalvaro – Marin and Machuca – Martinez. This is by far a practical system, which means that the system needs further optimization to achieve a fluidized state of the beads at lower flow rates. There are several design changes that can be made to improve this reactor further towards a higher DoD. For example, elongating the reactive zone to allow more catalyst to fit. By doing so we will decrease the LHSV, yielding a higher DoD. This however, will come with the drawback of additional pressure drop due to the longer bed [44]. Due to the higher flowrates required in this swirling fluidized bed reactor, the residence time in this reactor will not be long enough to achieve sufficiently high DoD in a single pass. Recirculation will probably be required, which will introduce back-mixing of unloaded DBT in the catalyst bed. This will lower the efficiency of the process; this is a trade-off with the increased mass and heat transfer than can be achieved by the swirling catalyst bed. Additional research is required in this field to find the optimum between a high flowrate which would increase swirling behaviour and increase mass and heat transfer, but these higher flowrates would require more recirculation passes, lowering the catalyst efficiency.

By decreasing the radius of the reactive zone there will be a stronger rotational acceleration on the particles, causing stronger swirling behaviour even at lower flow rate, which should increase residence time of the liquid in the fluidized regime. This increase in rotational force will likely also help with faster removal of the gas phase, leading towards a more efficient reaction [65].

A third design change we would propose to future systems is a way to eliminate the accumulation of the catalyst near the bottom plate of the reactor, for this we could use a conical shaped bottom plate, as is used on the bottom of most glass bottles. This would remove the dead zone inside the reactor and ensure that more of the catalyst is freely flowing, similar to the effect of a cone in a TORBED reactor [66].

In addition to the design changes for the reactive zone, the upper sections of the reactor should also be optimized to allow for quick degassing of the liquid, while keeping the total volume of the reactor low [67]. This would increase the power density of the total reactor system. Another factor that can help with the increased fluidization in the size of the catalyst beads. From Eq. 1, it can be seen that the diameter of the particle is inversely proportional to the U_{mf}, decreasing the size of the particle will therefor decrease the minimal flow rates required for the fluidization. This would also lead to longer residence time and improved DoD, while still having the added benefit of the increased mass and heat transfer that arises from fluidizing the beads [44].

4. Conclusion

In this work we presented a novel type of swirling reactor for the dehydrogenation of H18-DBT. The dehydrogenation reaction of this compound is characterized by large volumes of gas that are formed during the reaction, which reduces liquid and catalyst contact and reduces the overall efficiency of the H_2 release process. The endothermic reaction also impedes improved heat transfer schemes, which is also proposed via the swirling flow, and confirmed with the numerical results of the slip velocity, which reaches a maximal value of 0.4 m s^{-1}. As a prototyping study we presented this new reactor in a cold flow mock-up study. This study has shown that the swirling liquid flow, aided by the presence of a gas phase is crucial for the fluidization of the catalytic bed. The behaviour of this swirling reactor was illustrated by showing the fluidization of the particles both in an experimental setup and by CFD simulations (Euler-Euler) to characterize the flow behaviour numerically. It was shown both experimentally and with simulations that the beads in this three-phase system could easily exceed a height of 10 mm in the reactor, an increase in height of 7 mm compared to the initial bed height. This reactor allows of the beads to stay inside the reactive zone whilst having a liquid flow profile with little back mixing. The benefits of the fluidization of the catalyst beads are important in the dehydrogenation process as it allows for better removal of H_2 gas from the catalyst surface. Furthermore, the reactor also showed to aid in the removal of gas by concentrating the gas phase in the centre of the reactor and removing it from the active zone of the reactor. Although we did show that a system with similar hydrodynamic properties to a reacting H18-DBT mixture can be fluidized in our reactor, several design parameters should be optimized to make this reactor more effective to reach higher DoD.

Acknowledgement:

The authors thank the Port of Antwerp-Bruges as well as the University of Antwerp for the support to conduct this research. The authors gratefully acknowledge support of the Industrial Research Fund of the Antwerp University Association for the acquisition of the experimental setup used, and the University Research Fund (BOF) for the human resources. The computational resources and services used in this work were provided by the HPC core facility CalcUA of the Universiteit Antwerpen, and VSC (Flemish Supercomputer Centre), funded by the Research Foundation - Flanders (FWO) and the Flemish Government.

Declaration of competing interest

The authors declare that they have no known competing conflicts of interest.

References

1. Niermann, M., et al., *Liquid Organic Hydrogen Carriers and alternatives for international transport of renewable hydrogen.* Renewable and Sustainable Energy Reviews, 2021. **135**: p. 110171.
2. Narayanan, T.M., et al., *Role of Liquid Hydrogen Carriers in Deeply Decarbonized Energy Systems.* ACS Sustainable Chemistry & Engineering, 2022. **10**(33): p. 10768-10780.
3. Han, D.J., et al., *A Novel Eutectic Mixture of Biphenyl and Diphenylmethane as a Potential Liquid Organic Hydrogen Carrier: Catalytic Hydrogenation.* Energy Technology, 2019. **7**(1): p. 113-121.
4. Park, H., et al., *Hydrogen storage and release characteristics of polycyclic aromatic by-products for LOHC systems.* Applied Catalysis A: General, 2022. **636**: p. 118583.
5. Safronov, S.P., et al., *Reversible storage and release of hydrogen with LOHC: Evaluation of thermochemical data for methyl-quinolines with complementary experimental and computational methods.* Fuel, 2022. **317**: p. 123501.
6. Dong, Y., et al., *Study of catalytic hydrogenation and dehydrogenation of 2,3-dimethylindole for hydrogen storage application.* RSC Advances, 2021. **11**(26): p. 15729-15737.
7. Verevkin, S.P., et al., *Hydrogen Storage: Thermodynamic Analysis of Alkyl-Quinolines and Alkyl-Pyridines as Potential Liquid Organic Hydrogen Carriers (LOHC).* Applied Sciences, 2021. **11**(24): p. 11758.
8. Oh, J., et al., *2-(N-Methylbenzyl)pyridine: A Potential Liquid Organic Hydrogen Carrier with Fast H2 Release and Stable Activity in Consecutive Cycles.* ChemSusChem, 2018. **11**(4): p. 661-665.
9. Verevkin, S.P., R. Siewert, and A.A. Pimerzin, *Furfuryl alcohol as a potential liquid organic hydrogen carrier (LOHC): Thermochemical and computational study.* Fuel, 2020. **266**: p. 117067.
10. Jang, M., et al., *A study on hydrogen uptake and release of a eutectic mixture of biphenyl and diphenyl ether.* Journal of Energy Chemistry, 2020. **42**: p. 11-16.
11. Van Hoecke, L., et al., *Challenges in the use of hydrogen for maritime applications.* Energy & Environmental Science, 2021. **14**(2): p. 815-843.
12. Heublein, N., M. Stelzner, and T. Sattelmayer, *Hydrogen storage using liquid organic carriers: Equilibrium simulation and dehydrogenation reactor design.* International Journal of Hydrogen Energy, 2020. **45**(46): p. 24902-24916.
13. Modisha, P., et al. *A Promising Catalyst for the Dehydrogenation of Perhydro-Dibenzyltoluene: Pt/Al2O3 Prepared by Supercritical CO2 Deposition*. Catalysts, 2022. **12**, DOI: 10.3390/catal12050489.
14. Sisáková, K., et al., *Novel Catalysts for Dibenzyltoluene as a Potential Liquid Organic Hydrogen Carrier Use—A Mini-review.* Energy & Fuels, 2021. **35**(9): p. 7608-7623.
15. Müller, K., et al., *Liquid Organic Hydrogen Carriers: Thermophysical and Thermochemical Studies of Benzyl- and Dibenzyl-toluene Derivatives.* Industrial & Engineering Chemistry Research, 2015. **54**(32): p. 7967-7976.
16. Modisha, P., et al., *Evaluation of catalyst activity for release of hydrogen from liquid organic hydrogen carriers.* International Journal of Hydrogen Energy, 2019. **44**(39): p. 21926-21935.
17. Steinhauer, J., et al., *Model Catalytic Studies of Liquid Organic Hydrogen Carriers: Indole/Indoline/Octahydroindole on Ni(111).* The Journal of Physical Chemistry C, 2020. **124**(41): p. 22559-22567.
18. Modisha, P.M., et al., *The Prospect of Hydrogen Storage Using Liquid Organic Hydrogen Carriers.* Energy & Fuels, 2019. **33**(4): p. 2778-2796.
19. Perreault, P., et al., *Critical challenges towards the commercial rollouts of a LOHC-based H2 economy.* Current Opinion in Green and Sustainable Chemistry, 2023: p. 100836.
20. Jorschick, H., et al., *Charging a Liquid Organic Hydrogen Carrier with Wet Hydrogen from Electrolysis.* ACS Sustainable Chemistry & Engineering, 2019. **7**(4): p. 4186-4194.

21. Jorschick, H., et al., *Charging a Liquid Organic Hydrogen Carrier System with H2/CO2 Gas Mixtures.* ChemCatChem, 2018. **10**(19): p. 4329-4337.
22. Jorschick, H., et al., *Hydrogen storage using a hot pressure swing reactor.* Energy & Environmental Science, 2017. **10**(7): p. 1652-1659.
23. Biniwale, R.B., H. Yamashiro, and M. Ichikawa, *In-situ infrared thermographic analysis during dehydrogenationof cyclohexane over carbon-supported Pt catalysts using spray-pulsed reactor.* Catalysis Letters, 2005. **102**(1): p. 23-31.
24. Biniwale, R.B., N. Kariya, and M. Ichikawa, *Dehydrogenation of Cyclohexane Over Ni Based CatalystsSupported on Activated Carbon using Spray-pulsed Reactor and Enhancement in Activity by Addition of a Small Amount of Pt.* Catalysis Letters, 2005. **105**(1): p. 83-87.
25. Ali, J.K., E. Newson, and D. Rippin, *Exceeding equilibrium conversion with a catalytic membrane reactor for the dehydrogenation of methylcyclohexane.* Chemical engineering science, 1994. **49**(13): p. 2129-2134.
26. Wunsch, A., T. Berg, and P. Pfeifer, *Hydrogen Production from the LOHC Perhydro-Dibenzyl-Toluene and Purification Using a 5 µm PdAg-Membrane in a Coupled Microstructured System.* Materials, 2020. **13**(2).
27. Gora, A., et al., *Lower temperature dehydrogenation of methylcyclohexane by membrane-assisted equilibrium shift.* Chemistry letters, 2006. **35**(12): p. 1372-1373.
28. Geisselbrecht, M., et al., *Highly efficient, low-temperature hydrogen release from perhydro-benzyltoluene using reactive distillation.* Energy & Environmental Science, 2020. **13**(9): p. 3119-3128.
29. Rüde, T., et al., *Performance of continuous hydrogen production from perhydro benzyltoluene by catalytic distillation and heat integration concepts with a fuel cell.* Energy Technology. **n/a**(n/a).
30. Badakhsh, A., et al., *COX-free LOHC dehydrogenation in a heatpipe reformer highly integrated with a hydrogen burner.* Chemical Engineering Journal, 2022. **449**: p. 137679.
31. Bollmann, J., et al., *A path to a dynamic hydrogen storage system using a liquid organic hydrogen carrier (LOHC): Burner-based direct heating of the dehydrogenation unit.* International Journal of Hydrogen Energy, 2023. **48**(3): p. 1011-1023.
32. JINGWEN;, H.X., et al., *Centrifugal separation type dehydrogenation reactor and system based on heat pipe heat exchange*, X.J. UNIVERSITY, Editor. 2022, XIAN JIAOTONG UNIVERSITY.
33. Bösmann, A., et al., *Reactor device for the release of a gas from a starting material*. 2016, Hydrogenious Lohc Technologies GmbH.
34. Rathke, J., et al., *Reactor apparatus for dehydrogenating a carrier medium*. 2019, Hydrogenious Technologies GMBH: Germany.
35. Peters, R., et al., *A solid oxide fuel cell operating on liquid organic hydrogen carrier-based hydrogen – A kinetic model of the hydrogen release unit and system performance.* International Journal of Hydrogen Energy, 2019. **44**(26): p. 13794-13806.
36. Kuzmin, A.O., *Confined multiphase swirled flows in chemical engineering.* Reviews in Chemical Engineering, 2021. **37**(1): p. 31-68.
37. Solymosi, T., et al., *Nucleation as a rate-determining step in catalytic gas generation reactions from liquid phase systems.* Science Advances, 2022. **8**(46).
38. Brückner, N., et al., *Evaluation of Industrially Applied Heat-Transfer Fluids as Liquid Organic Hydrogen Carrier Systems.* ChemSusChem, 2014. **7**(1): p. 229-235.
39. Geburtig, D., et al., *Chemical utilization of hydrogen from fluctuating energy sources – Catalytic transfer hydrogenation from charged Liquid Organic Hydrogen Carrier systems.* International Journal of Hydrogen Energy, 2016. **41**(2): p. 1010-1017.
40. Wulf, C. and P. Zapp, *Assessment of system variations for hydrogen transport by liquid organic hydrogen carriers.* International Journal of Hydrogen Energy, 2018. **43**(26): p. 11884-11895.

41. van der Meer, E.H., R.B. Thorpe, and J.F. Davidson, *Dimensionless groups for practicable similarity of circulating fluidised beds.* Chemical Engineering Science, 1999. **54**(22): p. 5369-5376.
42. Knowlton, T.M., S.B.R. Karri, and A. Issangya, *Scale-up of fluidized-bed hydrodynamics.* Powder Technology, 2005. **150**(2): p. 72-77.
43. Fan, L.-S., *Chapter 2 - Hydrodynamics of Cocurrent Upward Fluidized Bed Systems (Modes E-I-a-1 and E-I-b; Figure 1.3)*, in *Gas–Liquid–Solid Fluidization Engineering*, L.-S. Fan, Editor. 1989, Butterworth-Heinemann: Boston. p. 33-161.
44. Kunii, D. and O. Levenspiel, *CHAPTER 3 - Fluidization and Mapping of Regimes*, in *Fluidization Engineering (Second Edition)*, D. Kunii and O. Levenspiel, Editors. 1991, Butterworth-Heinemann: Boston. p. 61-94.
45. Aslam, R., et al., *Thermophysical Studies of Dibenzyltoluene and Its Partially and Fully Hydrogenated Derivatives.* Journal of Chemical & Engineering Data, 2018. **63**(12): p. 4580-4587.
46. Hu, X., et al., *CFD simulations of stirred-tank reactors for gas-liquid and gas-liquid-solid systems using OpenFOAM®.* 2021. **19**(2): p. 193-207.
47. Ishii, M. and N. Zuber, *Drag coefficient and relative velocity in bubbly, droplet or particulate flows.* AIChE Journal, 1979. **25**(5): p. 843-855.
48. Asad, A., C. Kratzsch, and R. Schwarze, *Influence of drag closures and inlet conditions on bubble dynamics and flow behavior inside a bubble column.* Engineering Applications of Computational Fluid Mechanics, 2017. **11**(1): p. 127-141.
49. Li, C., et al., *A Study of Drag Force in Isothermal Bubbly Flow.* The Journal of Computational Multiphase Flows, 2009. **1**(4): p. 295-309.
50. Foundation, T.O. *IshiiZuber Class Reference*. C++ Source Code Guide 2020 01-09-2022]; Available from: https://cpp.openfoam.org/v8/classFoam_1_1dragModels_1_1IshiiZuber.html#details.
51. Vandewalle, L.A., et al., *Process Intensification in a Gas–Solid Vortex Unit: Computational Fluid Dynamics Model Based Analysis and Design.* Industrial & Engineering Chemistry Research, 2019. **58**(28): p. 12751-12765.
52. Ergun, S. *Fluid flow through packed columns*. 1952.
53. Wen, C.-Y.Y., Y.H., *Mechanics of fluidization.* Chemical Engineering Progress Symposium Series, 1966. **62**.
54. Tabib, M.V. and P. Schwarz, *Quantifying sub-grid scale (SGS) turbulent dispersion force and its effect using one-equation SGS large eddy simulation (LES) model in a gas–liquid and a liquid–liquid system.* Chemical Engineering Science, 2011. **66**(14): p. 3071-3086.
55. Menter, F.R., *Two-equation eddy-viscosity turbulence models for engineering applications.* AIAA Journal, 1994. **32**(8): p. 1598-1605.
56. Van Cauwenberge, D.J., et al., *CFD-based design of 3D pyrolysis reactors: RANS vs. LES.* Chemical Engineering Journal, 2015. **282**: p. 66-76.
57. Bestion, D., *The difficult challenge of a two-phase CFD modelling for all flow regimes.* Nuclear Engineering and Design, 2014. **279**: p. 116-125.
58. Larsen, B.E., D.R. Fuhrman, and J. Roenby, *Performance of interFoam on the simulation of progressive waves.* Coastal Engineering Journal, 2019. **61**(3): p. 380-400.
59. Roache, P.J., *Perspective: A Method for Uniform Reporting of Grid Refinement Studies.* Journal of Fluids Engineering, 1994. **116**(3): p. 405-413.
60. Van Hoecke, L., et al., *Experimental methods in chemical engineering: Computational fluid dynamics/finite volume method–CFD/FVM.* The Canadian Journal of Chemical Engineering, 2022. **n/a**(n/a).
61. Park, S., M. Naseem, and S. Lee, *Experimental Assessment of Perhydro-Dibenzyltoluene Dehydrogenation Reaction Kinetics in a Continuous Flow System for Stable Hydrogen Supply.* Materials, 2021. **14**(24).

62. Wang, J., et al., *Review of (gas)-liquid-solid circulating fluidized beds as biochemical and environmental reactors.* Chemical Engineering Journal, 2020. **386**: p. 121951.
63. Otálvaro-Marín, H.L. and F. Machuca-Martínez, *Sizing of reactors by charts of Damköhler's number for solutions of dimensionless design equations.* Heliyon, 2020. **6**(11): p. e05386.
64. Bulgarin, A., et al., *Purity of hydrogen released from the Liquid Organic Hydrogen Carrier compound perhydro dibenzyltoluene by catalytic dehydrogenation.* International Journal of Hydrogen Energy, 2020. **45**(1): p. 712-720.
65. Grimstad, A.-A., et al., *Degassing Rate of Drilling Fluid Base Oils as Exposed to Depressurisation and Drill String Rotation*, in *SPE/IADC Drilling Conference and Exhibition*. 2017. p. D032S025R002.
66. Blissett, R., et al., *Valorisation of rice husks using a TORBED® combustion process.* Fuel Processing Technology, 2017. **159**: p. 247-255.
67. Liu, L., et al., *Analysis of Hydrocyclone Geometry via Rapid Optimization Based on Computational Fluid Dynamics.* Chemical Engineering & Technology, 2021. **44**(9): p. 1693-1707.